

A New Efficient Method of Hartree-Fock-Bogoliubov Calculation for Weakly Bound Nuclei

M. Stoitsov

*Department of Physics, Graduate School of Science, Kyoto University, Kyoto 606-8502, Japan
Department of Physics and Astronomy, University of Tennessee, Knoxville, Tennessee 37996, USA
Physics Division, Oak Ridge National Laboratory,
P.O. Box 2008, Oak Ridge, Tennessee 37831, USA and
Institute of Nuclear Research and Nuclear Energy,
Bulgarian Academy of Sciences, Sofia-1784, Bulgaria*

N. Michel and K. Matsuyanagi

*Department of Physics, Graduate School of Science, Kyoto University, Kyoto 606-8502, Japan
(Dated: January 26, 2023)*

We propose a new method to solve the Hartree-Fock-Bogoliubov equations for weakly bound nuclei, which works for both spherical and axially deformed cases. In this approach, the quasiparticle wave functions are expanded in a complete set of analytical Pöschl-Teller-Ginocchio and Bessel/Coulomb wave functions. Correct asymptotic properties of the quasiparticle wave functions are endowed in the proposed algorithm. Good agreement is obtained with the results of the Hartree-Fock-Bogoliubov calculation using the box boundary condition for a set of benchmark spherical and deformed nuclei.

PACS numbers: 21.10.-k, 21.30.+y, 21.60.Jz

Keywords:

I. INTRODUCTION

The study of nuclei far from stability is an increasingly important part of contemporary nuclear physics. This topic is related to newly created radioactive beam facilities, allowing more experiments on nuclei beyond the stability line. The new experimental opportunities on nuclei with extreme isospin ratio and weak binding bring new phenomena which inevitably require a universal theoretical description of nuclear properties for all nuclei. The current approach to the problem is the nuclear density functional theory which implicitly relies on Hartree-Fock-Bogoliubov (HFB) theory, unique in its ability to span the whole nuclear chart.

The HFB equations can be solved in coordinate space using the box boundary condition [1, 2]. This approach (abbreviated HFB/Box in this paper) has been used as a standard tool in the description of spherical nuclei [3]. Its implementation to systems with deformed equilibrium shapes is much more difficult, however. Different approaches have been developed to deal with this problem, such as the two-basis method [4, 5, 6], the canonical-basis framework [7, 8, 9], and basis-spline techniques in coordinate-space calculations developed for axially symmetric nuclei [10, 11]. These algorithms are precise, but time-consuming.

Configuration-space HFB diagonalization is a useful alternative to coordinate-space calculations whereby the HFB solution is expanded in a complete set of single-particle states. In this context, the harmonic oscillator (HO) basis turned out to be particularly useful. Over the years, many configuration-space HFB codes using the HO basis (abbreviated HFB/HO) have been developed,

employing either the Skyrme or the Gogny effective interactions [12, 13, 14, 15, 16, 17], or using a relativistic Lagrangian [19] in the context of the relativistic Hartree-Bogoliubov theory. In the absence of fast coordinate-space methods to obtain deformed HFB solutions, the configuration-space approach has proved to be a very fast and efficient alternative, allowing large-scale calculations [17, 18].

Close to drip lines, however, the continuum states start playing an increasingly important role, and it becomes necessary to treat the interplay of both continuum and deformation effects in an appropriate manner. Unfortunately, none of the existing configuration-space HFB techniques manage to incorporate continuum effects.

The goal of the present work is to find an efficient numerical scheme to solve HFB equations for spherical and axially deformed nuclei which properly takes the continuum effects into account. We will denote this problem as continuum HFB (CHFB). Aiming at treating spherical and deformed nuclei on the same footing, we rely on the configuration-space HFB approach.

The HO basis has important numerical advantages; for example, the use of the Gauss-Hermite quadrature allows fast evaluation of matrix elements. On the other hand, its Gaussian asymptotics prevents the expansion of systems with large spatial extension, such as halo nuclear states. This problem can be successfully fixed by using the transformed HO basis (THO) [20]. The latter transforms the unphysical Gaussian fall-off of HO states into a more physical exponential decay. Neither HO nor THO bases, however, are able to provide proper discretization of the quasiparticle continuum.

Obviously, a more practical basis is needed. The

Gamow Hartree-Fock (GHF) basis [21] would be appropriate, as it has been demonstrated that it can provide the correct asymptotic of loosely bound nuclear states. However, it implies the use of complex symmetric matrices. Moreover, the presence of basis states, which increase exponentially in modulus, leads to numerical divergences, unless the costly two-basis method is employed [30].

As we plan to consider bound HFB ground states only, it is more advantageous numerically to employ Hermitian completeness relations, whose radial wave functions are real. They are either bound, thus integrable, or oscillate with almost constant amplitude, so that we are free from the numerical cancellation problems associated with the Gamow states. It should be stressed that we can generate a Gamow quasiparticle basis using the HFB potentials thus obtained. We can then describe resonant excited states by means of the quasiparticle random phase approximation (QRPA) representing the QRPA matrix elements in terms of the Gamow quasiparticle basis. This serves as an interesting subject for future investigation.

One could expect that the employment of the spherical Hartree-Fock (HF) potential to generate the real continuum HF (CHF) complete basis would solve the problem. Unfortunately, the CHF basis is not numerically stable due to the presence of resonances in the vicinity of the real continuum. The continuum states lying close to a narrow resonance are rapidly changing, so that a very dense continuum discretization around this resonance is necessary to accurately represent this energy region. Important numerical cancellations would occur as continuum wave functions become very large in amplitude close to narrow resonances.

To overcome this difficulty, we adopt a technique based on the exactly solvable Pöschl-Teller-Ginocchio (PTG) potential [22]. The spherical HF potential, seemingly the best candidate to generate a rapidly converging basis expansion, but providing numerically costly GHF bases or unstable CHF bases, is replaced by a PTG potential fitted to the HF potential if the latter give rise to resonant structure. It will be shown that the narrow resonant states of the GHF basis will become bound in the PTG basis, so that its scattering states will have no rapid phase shift change, a necessary condition for numerically stable continuum discretization. As a result, we obtain a very good basis for HFB calculations. We call this approach HFB/PTG.

To test the feasibility of this new method, we have performed numerical calculations for spherical Ni isotopes near the drip line, $^{84}\text{Ni} - ^{90}\text{Ni}$, for a strongly deformed nucleus ^{110}Zr , and two HF solutions for ^{40}Mg with different (prolate and oblate) deformations. Good agreement with box-discretized continuum calculations is obtained.

This paper is organized as follows. The HFB/PTG algorithm is described in Sec. II, while the method used to generate the PTG basis is formulated in Sec. III. Asymptotic properties of the HFB quasiparticle wave functions are discussed in Sec. IV. Results of numerical calculation

are presented in Sec. V. A brief summary and conclusions are given in Sec. VI. Some technical details related to the PTG basis and calculation of matrix elements are collected in Appendices.

II. THE HFB/PTG APPROACH

Our aim is to develop an efficient method of solving the CHF equation

$$\int d\mathbf{r}' \sum_{\sigma'} \begin{pmatrix} h(\mathbf{r}\sigma, \mathbf{r}'\sigma') - \lambda & \tilde{h}(\mathbf{r}\sigma, \mathbf{r}'\sigma') \\ \tilde{h}(\mathbf{r}\sigma, \mathbf{r}'\sigma') & -h(\mathbf{r}\sigma, \mathbf{r}'\sigma') + \lambda \end{pmatrix} \times \begin{pmatrix} U(E, \mathbf{r}'\sigma') \\ V(E, \mathbf{r}'\sigma') \end{pmatrix} = E \begin{pmatrix} U(E, \mathbf{r}\sigma) \\ V(E, \mathbf{r}\sigma) \end{pmatrix} \quad (1)$$

for weakly bound nuclei, which equally works for both spherical and axially deformed nuclei. In the above equation, \mathbf{r} and σ are the coordinates of the particle in normal and spin space, $h(\mathbf{r}\sigma, \mathbf{r}'\sigma')$ and $\tilde{h}(\mathbf{r}\sigma, \mathbf{r}'\sigma')$ denote the particle-hole and the particle-particle (hole-hole) components of the single-particle Hamiltonian, respectively, $U(\mathbf{r}\sigma)$ and $V(\mathbf{r}\sigma)$ are the upper and the lower components of the single-quasiparticle wave function, and λ is the chemical potential [3]. For simplicity of notation, the isospin index q is omitted in Eq. (1), but, of course, we solve the CHF equation for coupled systems of protons and neutrons. In this section, we outline the calculational scheme, and details will be presented in the succeeding sections.

The proposed method to solve the CHF equations, abbreviated HFB/PTG, consists of the following steps:

(1) One starts with spherical or deformed HFB calculations in the HO basis (HFB/HO). This provides a good approximate solution for the HF potential and the effective mass.

(2) One considers a HF potential and an effective mass for each ℓj subspace, and fits the associated shifted PTG potential to them when the HF potential possesses bound or narrow resonant states in this ℓj subspace (see Sec. III A). If no such states appear in the HF ℓj spectrum, a set of Bessel/Coulomb wave functions [23] is selected for the ℓj partial wave basis.

(3) One diagonalizes the HFB eigenvalue equations in the basis composed of the PTG and Bessel/Coulomb wave functions. This step continues until self-consistency is achieved.

The use of the Bessel/Coulomb wave functions in step (2) occurs for partial waves of high angular momentum, for which the centrifugal part becomes dominant. As no resonant structure can appear therein in the real HF continuum, Bessel/Coulomb wave functions provide a numerically stable set of states for this partial wave. For the generation of Coulomb wave functions, one can use the recently published C++ code [24] or its FORTRAN alternative [25]. A complete set of wave functions is thus formed, which will be used as a basis to expand the HFB quasiparticle wave functions.

The necessary truncation of the basis in step (3) implies that spurious effects may eventually appear at very large distances, where both the particle density ρ and the pairing density $\tilde{\rho}$ are very small. Consequently, quasiparticle wave functions have to be matched to their exact asymptotics at moderate distances as it is explained further in Sec. IV. In addition, special care must be taken to calculate matrix elements due to the presence of non-integrable scattering states (see Appendix B).

When the HF mean field resulting from the HFB/HO calculation in step (1) is deformed, there are several ways to extract the HF potential for each ℓj subspace to be used in step (2). Because it is used just as a generator for the complete PTG basis, its choice will have little effect on the final HFB solution, however. In the present calculation, we therefore adopt a simple procedure; the particle-hole part of the HFB/HO potential and the HFB/HO effective mass are used in step (2) after averaging their angular and spin degrees of freedom. The resulting HF potential is spherical and the same for all ℓj subspaces. In such a case, the effect of the spin-orbit splitting is not taken into account in the stage of constructing the PTG basis, but it is, of course, taken into account in step (3).

III. GENERATION OF BASIS

A. PTG potentials fitting procedure

The PTG potential has four parameters Λ , s , ν , and a , which have to be determined in each ℓj subspace (see Appendix A). For this purpose, we use the spherical HF potential and effective mass in a given ℓj subspace.

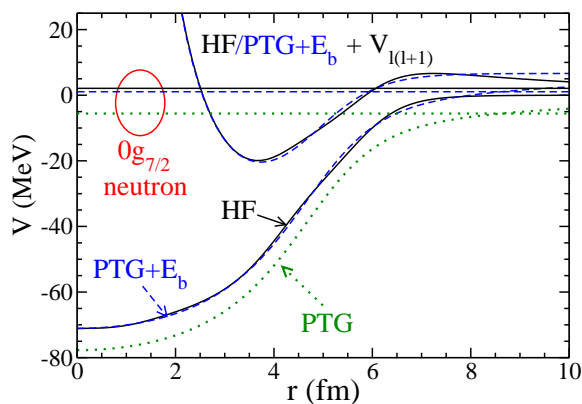


FIG. 1: (color online) The shifted PTG potential (dashed lines), the HF potential (solid lines) calculated with the SLy4-force, and the unshifted PTG potential (dotted line) for neutrons in ^{84}Ni . The energies of the $0g_{7/2}$ levels for these potentials are indicated.

The PTG mass parameter a is obtained from the re-

quirement that the PTG and the HF effective masses are the same at the origin. One first adds the centrifugal term $V_{l(l+1)} \propto \ell(\ell+1)/r^2$ to the nuclear plus Coulomb potential, $V_N + V_C$, and determines the height E_b of the centrifugal (plus Coulomb) barrier. Then, one adds E_b to the PTG potential; the resulting potential may be called the shifted PTG potential. The parameters Λ and ν are fitted in such a way that the χ^2 difference between the shifted PTG potential and the HF potential is minimal. Note that s is directly obtained from Λ and ν values during the fit, as it is determined by way of the property that the PTG potential of parameters Λ , s , ν , and a for $r \rightarrow 0$ is equivalent to s^2 times the PTG potential of parameters Λ , $s = 1$, ν and a . The reason why we use the barrier height E_b in our fitting procedure will become apparent by an illustrative example presented below.

To test the fitting procedure and the quality of the resulting PTG basis, we performed GHF calculations in the coordinate space for the spherical nucleus ^{84}Ni . Let us examine the quality of single-particle energies and wave functions resulting from the shifted PTG potential by comparing them with the GHF energies and wave functions for bound and resonance states.

Figure 1 illustrates the PTG fitting procedure and compares the results with the GHF ones taking the neutron $0g_{7/2}$ level as an example. It is seen that the energy of the bound $0g_{7/2}$ state in the original (unshifted) PTG potential (horizontal dotted line) becomes positive after being shifted with E_b (horizontal dashed line), and its position agrees in a good approximation with the resonance energy obtained by the GHF calculation (horizontal solid line). In this case, the PTG treatment replaces the GHF resonance with a weakly bound PTG state whose wave function will be very similar in the nuclear region. Thus, one can expect that the fitted PTG potential provides a rapidly converging basis for solving the HFB equations.

In fact, it is not necessary to find the PTG potential that exactly minimizes the χ^2 difference with the HF potential. As the PTG potential is used as a basis generator, slight differences with the exact minimum lead only to slightly different basis states to expand the HFB quasiparticle wave functions, preserving its rapidly converging properties. Thus, one can take rather large steps for the Λ , ν variations and few radii for the χ^2 evaluation to save computer time, keeping the quality of the basis essentially the same.

B. Single-particle energies

Single-particle energies and widths for neutrons in ^{84}Ni , obtained by the GHF calculations, are compared with the PTG energies in Table I. One can clearly see the following facts.

Firstly, the overall agreement between the GHF and the shifted PTG energies is good, which means that the PTG potential is flexible enough to reproduce the main features of the HF potential.

Secondly, all narrow GHF resonances are represented as weakly bound PTG states with upward shifted PTG energies. This is very important because the HFB quasiparticle states are likely to have large overlaps with narrow resonance states.

We note that the GHF states whose width is larger than 1 MeV, as a rule, are not converted to bound PTG states. This is not important, however, because scattering states do not exhibit rapid changes in the energy region of broad resonances. The broad resonance region can indeed be well represented in terms of the continuum basis states.

TABLE I: Neutron GHF levels in ^{84}Ni calculated with the SLy4 Skyrme-force and the surface-type delta pairing interaction (see Sec. V for the parameters used), which are compared with the PTG estimates. All energies are given in MeV while the widths Γ are given in keV.

states	GHF		PTG	
	Γ	e	$e + E_b$	e
$0s_{1/2}$	0	-52.38	-51.89	-51.89
$1s_{1/2}$	0	-24.37	-25.55	-25.55
$2s_{1/2}$	0	-0.72	-0.97	-0.97
$0p_{3/2}$	0	-41.25	-40.67	-41.09
$1p_{3/2}$	0	-12.52	-12.95	-13.36
$0p_{1/2}$	0	-39.44	-38.79	-39.22
$1p_{1/2}$	0	-10.67	-10.73	-11.16
$0d_{5/2}$	0	-29.38	-29.50	-31.02
$1d_{5/2}$	0	-1.90	-1.94	-3.46
$0d_{3/2}$	0	-25.20	-25.53	-27.11
$1d_{3/2}$	10.03	0.18	0.24	-1.34
$0f_{7/2}$	0	-17.56	-17.45	-20.88
$0f_{5/2}$	0	-10.87	-12.40	-16.01
$0g_{9/2}$	0	-6.11	-5.52	-11.74
$0g_{7/2}$	31.62	2.09	1.05	-5.58
$0h_{11/2}$	92.93	4.53	6.18	-3.79

C. PTG wave functions

As illustrated in Fig. 2, narrow GHF resonant states bear large overlaps with their associated PTG bound states. Hence, the GHF resonant structure present in the HFB quasiparticle wave functions will be sustained by the PTG bound states, thus reducing the coupling to the PTG scattering continuum.

An example indicating the quality of the bound single-particle wave functions resulting from the fitting PTG procedure is shown in Fig. 3 for the bound $0s_{1/2}$, $1s_{1/2}$, and $2s_{1/2}$ neutron states. In this case, the nuclear potential has no centrifugal barrier, so that the PTG and the HF potentials possess the same asymptotic behavior. Very good agreement between the PTG (dashed lines) and the GHF (solid lines) wave functions is thus not sur-

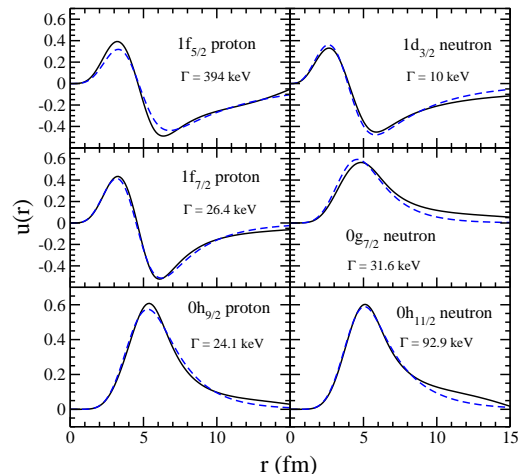


FIG. 2: (color online) The PTG (dashed lines) and GHF (solid lines) wave functions for various resonance states.

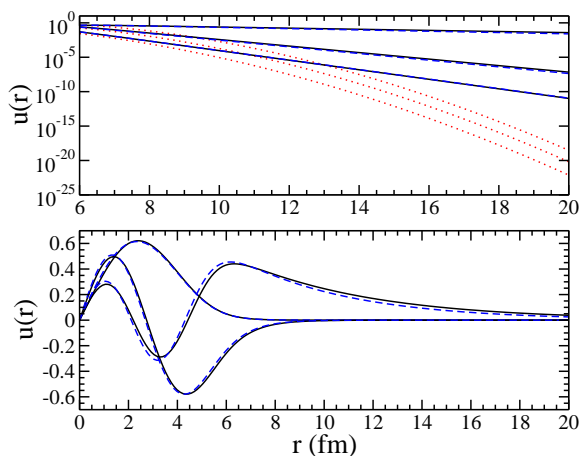


FIG. 3: (color online) The PTG (dashed lines), GHF (solid lines), and HO (dotted lines) wave functions including the asymptotic region for the bound $0s_{1/2}$, $1s_{1/2}$, and $2s_{1/2}$ neutron states both in normal scale (lower panel) and logarithmic scale (upper panel).

prising. The upper panel in Fig. 3 shows the asymptotic region in logarithmic scale where HO wave functions (dotted lines) are also given as a reference. Their Gaussian asymptotics cannot reproduce even approximately the exponential decrease of the PTG and GHF wave functions.

Neutron continuum s -states are illustrated in Fig. 4, which are properly reproduced as well by the scattering states for the PTG potential. In the cases when a centrifugal (and/or Coulomb) barrier exists, as illustrated in Fig. 5 for $d_{3/2}$ states, different phase shifts develop in the PTG and GHF continuum states, as the PTG potential decreases exponentially at large distance. This explains the small differences between the two PTG and GHF wave functions of largest energies. The remaining wave

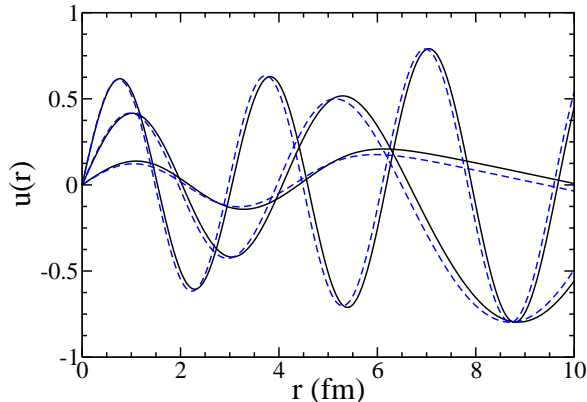


FIG. 4: (color online) The PTG (dashed lines) and GHF (solid lines) wave functions for the neutron continuum s -states.

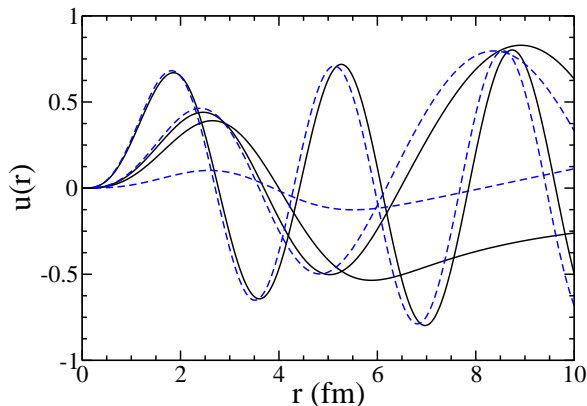


FIG. 5: (color online) The PTG (dashed lines) and the GHF (solid lines) wave functions for the neutron continuum $d_{3/2}$ -states.

functions, however, are different already in the vicinity of $r = 0$. This is because wave functions are normalized to a Dirac delta distribution. The constant induced by this normalization depends on the content of ingoing and outgoing wave functions, which are different in the PTG and GHF cases (exponential functions for the former, Hankel functions for the latter). They differ especially in the low energy region, which explains the difference of PTG and GHF low-energy wave function by roughly an overall multiplicative factor.

IV. QUASIPARTICLE WAVE FUNCTIONS IN THE ASYMPTOTIC REGION

The necessary truncation of the basis implies that spurious effects will eventually appear at a very large radius,

where both the particle density ρ and the pairing density $\tilde{\rho}$ are very small. Consequently, quasiparticle wave functions have to be matched with their exact asymptotics at a moderate distance, where the asymptotic region has been attained and densities are still large enough for basis expansion to be precise. Below we explain how the matching procedure is done for axially deformed nuclei.

In order to deal with the asymptotics of quasiparticle wave functions, we make partial wave decomposition of them:

$$U_{km}(\mathbf{r}\sigma) = \sum_{\alpha} U_{km}^{\alpha} \Psi_{\alpha}(\mathbf{r}) = \sum_{\ell j} U_{km}^{(\ell j)}(r) \mathcal{Y}_{km}^{\ell j}(\Omega),$$

$$V_{km}(\mathbf{r}\sigma) = \sum_{\alpha} V_{km}^{\alpha} \Psi_{\alpha}(\mathbf{r}) = \sum_{\ell j} V_{km}^{(\ell j)}(r) \mathcal{Y}_{km}^{\ell j}(\Omega),$$
(2)

where the subscript k specifies the quasiparticle eigenstates together with the magnetic quantum number m , which is always conserved for both spherical and axially symmetric nuclei; $\Psi_{\alpha}(\mathbf{r})$ are the PTG or Bessel/Coulomb wave functions; U_{km}^{α} and V_{km}^{α} are the HFB expansion coefficients; $U_{km}^{(\ell j)}(r)$ and $V_{km}^{(\ell j)}(r)$ are the radial amplitudes with $r = |\mathbf{r}|$ for the (ℓj) partial wave; $\mathcal{Y}_m^{\ell j}(\Omega)$ denotes a product wave function where the spherical harmonics with the angular variables Ω and the orbital angular momentum ℓ is coupled with spin to the total angular momentum j .

The partial wave amplitudes, $U_{km}^{(\ell j)}(r)$ and $V_{km}^{(\ell j)}(r)$ defined above, involve summation over all quantum numbers except the angular momenta ℓ and j . In the spherical case, the sums reduce to a single element, as ℓ and j are good quantum numbers. In the asymptotic region, only Coulomb and centrifugal parts remain from the HFB potentials, so that one can continue the quasiparticle wave functions via their partial wave decompositions and decay constants k_u and k_v :

$$U_{km}^{(\ell j)}(r) = C_{km}^{(\ell j)+} H_{\ell, \eta_u}^{+}(k_u r) + C_{km}^{(\ell j)-} H_{\ell, \eta_u}^{-}(k_u r),$$

$$V_{km}^{(\ell j)}(r) = D_{km}^{(\ell j)+} H_{\ell, \eta_v}^{+}(k_v r),$$
(3)

$$k_v = \sqrt{\frac{2m}{\hbar^2}(\lambda - E)}, k_u = \sqrt{\frac{2m}{\hbar^2}(\lambda + E)},$$

where E denotes the quasiparticle energy, λ the chemical potential, $H_{\ell, \eta}^{\pm}$ the Hankel (or Coulomb) functions, η being the Sommerfeld parameter, and $C_{km}^{(\ell j)+}$, $C_{km}^{(\ell j)-}$ and $D_{km}^{(\ell j)+}$ are constants to be determined. Matching is performed using Eq. (2) at a radius R_0 in the asymptotic region where the basis expansion is precise, so that $C_{km}^{(\ell j)+}$, $C_{km}^{(\ell j)-}$, and $D_{km}^{(\ell j)+}$ come forward by continuity. The value of R_0 is typically of the order of 10 fm.

TABLE II: Results of the HFB/PTG calculation for ground state characteristics of Ni isotopes close to the neutron drip line, which are compared with results of the HFB/Box calculation. The SLy4 functional and the surface-type delta pairing are used (see text). The rms radii are in fm and all other quantities are in MeV. Proton chemical potential λ_p is not provided as pairing correlations vanish in the proton space.

	^{84}Ni		^{86}Ni		^{88}Ni		^{90}Ni	
	HFB/Box	HFB/PTG	HFB/Box	HFB/PTG	HFB/Box	HFB/PTG	HFB/Box	HFB/PTG
λ_n	-1.453	-1.429	-1.037	-1.029	-0.671	-0.661	-0.342	-0.329
r_n	4.451	4.450	4.528	4.526	4.603	4.602	4.677	4.674
r_p	3.980	3.981	4.001	4.001	4.021	4.021	4.043	4.043
Δ_n	1.481	1.532	1.667	1.658	1.790	1.780	1.899	1.892
E_n^{pair}	-30.70	-30.60	-36.52	-35.92	-41.98	-41.187	-47.158	-46.233
T_n	1084.53	1085.95	1118.65	1118.63	1150.71	1150.64	1182.52	1182.66
T_p	430.47	430.240	425.99	426.01	421.71	421.72	417.38	417.37
E_n^{so}	-63.379	-63.177	-61.679	61.707	-59.558	59.681	-56.898	-57.889
E_{dir}^{Coul}	132.94	132.90	132.26	132.246	131.571	131.578	130.947	130.886
E_{exc}^{Coul}	-10.138	10.136	-10.084	-10.085	-10.033	10.033	-9.980	-9.980
E_{tot}	-654.89	-654.914	-656.933	-656.877	-658.167	-658.084	-658.665	-658.608

V. NUMERICAL EXAMPLES

We have made a feasibility test of the HFB/PTG method for spherical Ni isotopes close to the neutron drip line and for deformed neutron-rich nuclei ^{110}Zr and ^{40}Mg . All calculations were done using the SLy4 density functional. For the pairing interaction, we use the surface-type delta pairing with the strength $t'_0 = -519.9$ MeV fm^3 for the density-independent part and $t'_3 = -37.5t'_0$ MeV fm^6 for the density-dependent part with a sharp energy cut-off at 60 MeV in the quasiparticle space. They have been fitted to reproduce the neutron pairing gap of ^{120}Sn . These values are consistent with those given in Ref. [31]; the slight difference is due to different cut-off procedures, sharp cut-off in our case, and smooth cut-off in Ref. [31]. Below we discuss the major features of the results of calculation. We also make a detailed comparison between the HFB/PTG and HFB/Box calculations.

A. Spherical nuclei

Let us first examine how the results of calculation depend on the truncation of the basis. Indeed, the basis has to be truncated at a maximal linear momentum k_{max} , and discretized with N_{ℓ_j} continuum states per partial wave in the interval $[0 : k_{max}]$. Figure 6 shows that the use of values larger than $k_{max} = 3 \text{ fm}^{-1}$ does not change the results. Accordingly, in calculations for spherical nuclei, we use $k_{max} = 5 \text{ fm}^{-1}$ and discretize the continuum with $N_{\ell_j} = 60$ scattering states per partial wave (see Ref. [21] for its justification).

Results of the HFB/PTG calculation for a set of benchmark Ni isotopes close to the neutron drip line are presented in Table II and Fig. 7, where results of

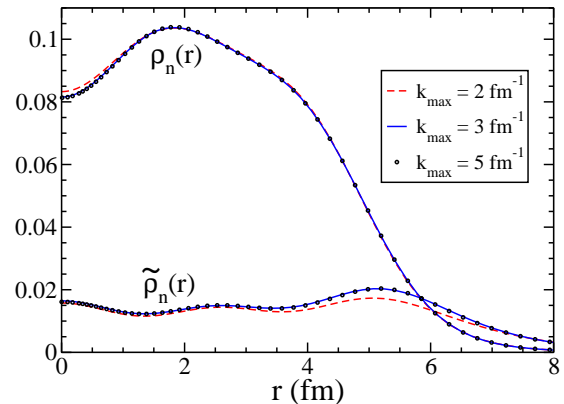


FIG. 6: (color online) Dependence on k_{max} of the neutron density ρ_n and the neutron pairing density $\tilde{\rho}_n$ calculated for ^{84}Ni by the HFB/PTG method.

the HFB/Box calculation are also shown for comparison. The Ni isotopes are spherical with pairing in the neutron channel only. We see immediately a remarkable agreement between the results of the HFB/PTG and HFB/Box calculations. The difference in total energies is less than 85 keV and the proton rms radii agree almost perfectly, while the neutron ones are slightly different by less than 0.003 fm. Similarly good agreement is obtained for all other energy counterparts. The good agreement in the ground state characteristics evaluated by the two different approaches is not surprising if one compares the density distributions shown in Fig. 7. In this figure, the neutron and proton densities, ρ_n and ρ_p , and the neutron pairing density $\tilde{\rho}_n$, are plotted both in normal (left col-

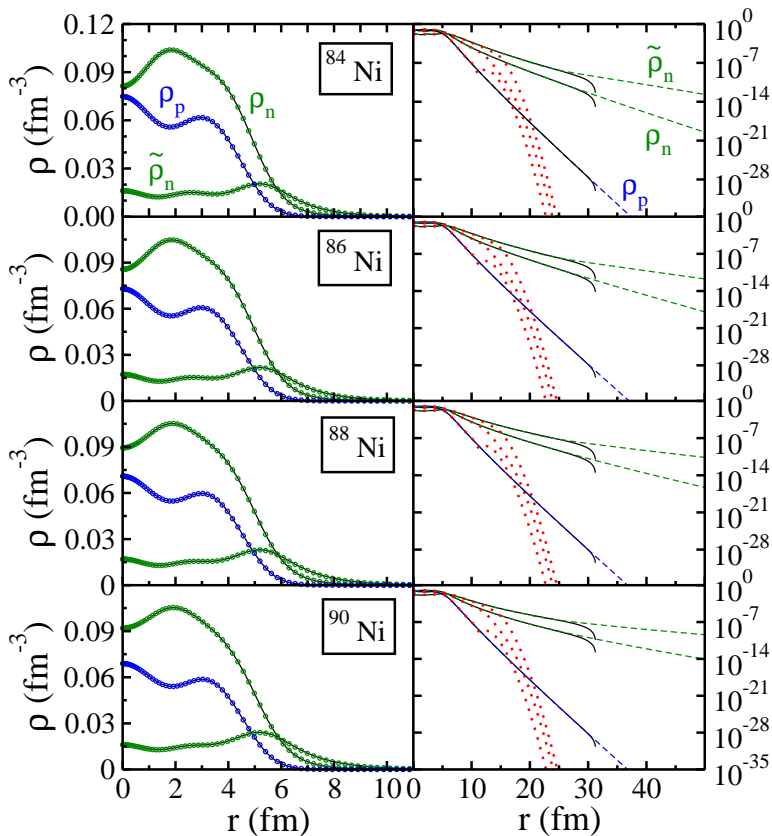


FIG. 7: (color online) The neutron densities ρ_n , the proton densities ρ_p , and the neutron pairing density $\tilde{\rho}_n$ both in normal (left-hand side) and logarithmic (right-hand side) scales. There are no pairing correlations in the proton channel. Results of the HFB/Box calculation are displayed by solid lines, while those of the HFB/PTG calculations are displayed by open circles and dashed lines. The HFB/HO densities are also indicated by dotted lines in the right panels for comparison.

umn) and logarithmic (right column) scales. The agreement is almost perfect in the whole range of r except at the box boundary where the HFB/Box densities vanish due to the boundary conditions. This agreement is striking considering the significant impact of the continuum for these nuclei and the fact that the HFB/PTG calculations are nevertheless performed using the basis expansion method.

Special attention has to be paid to the agreement for the pairing quantities. Interestingly, the pairing gap Δ_n increases as one approaches the drip line, indicating the important role of the pairing correlations in the continuum. This result is somehow different from that of Ref. [28] obtained by an alternative HFB calculation in the coordinate space for the same set of nuclei, but it is in agreement with the estimates from Ref. [29].

B. Axially deformed nuclei

In the case of axially deformed nuclei, few HFB/Box calculations are available to check the HFB/PTG results. We consider the well-deformed nucleus ^{110}Zr (deformation $\beta \approx 0.4$), already studied in Ref.[26], and two

states with different deformations for the drip line nucleus ^{40}Mg . We use therein $k_{max} = 4 \text{ fm}^{-1}$ and $N_{\ell j} = 30$ for all partial waves.

Table III compares the three approaches with respect to ground state properties of ^{110}Zr . In general they yield similar values. The differences seen in Table III are partially due to the different structure of the model spaces adopted and the associated fitting of the pairing strength.

TABLE III: Comparison of ground state properties of ^{110}Zr calculated with the HFB/Box, HFB/PTG, and HFB/THO approaches. The rms radii are in fm, quadrupole moments are in barn, and all other quantities are in MeV.

	HFB/Box	HFB/PTG	HFB/THO
Q_{tot}	12.088	12.53	12.303
Δ_n	0.480	0.626	0.562
E_n^{pair}	-1.53	-3.015	-2.05
r_n	4.82	4.836	4.831
r_p	4.55	4.560	4.556
E_{tot}	-893.93	-893.952	-893.711

A comparison for both proton and neutron densities,

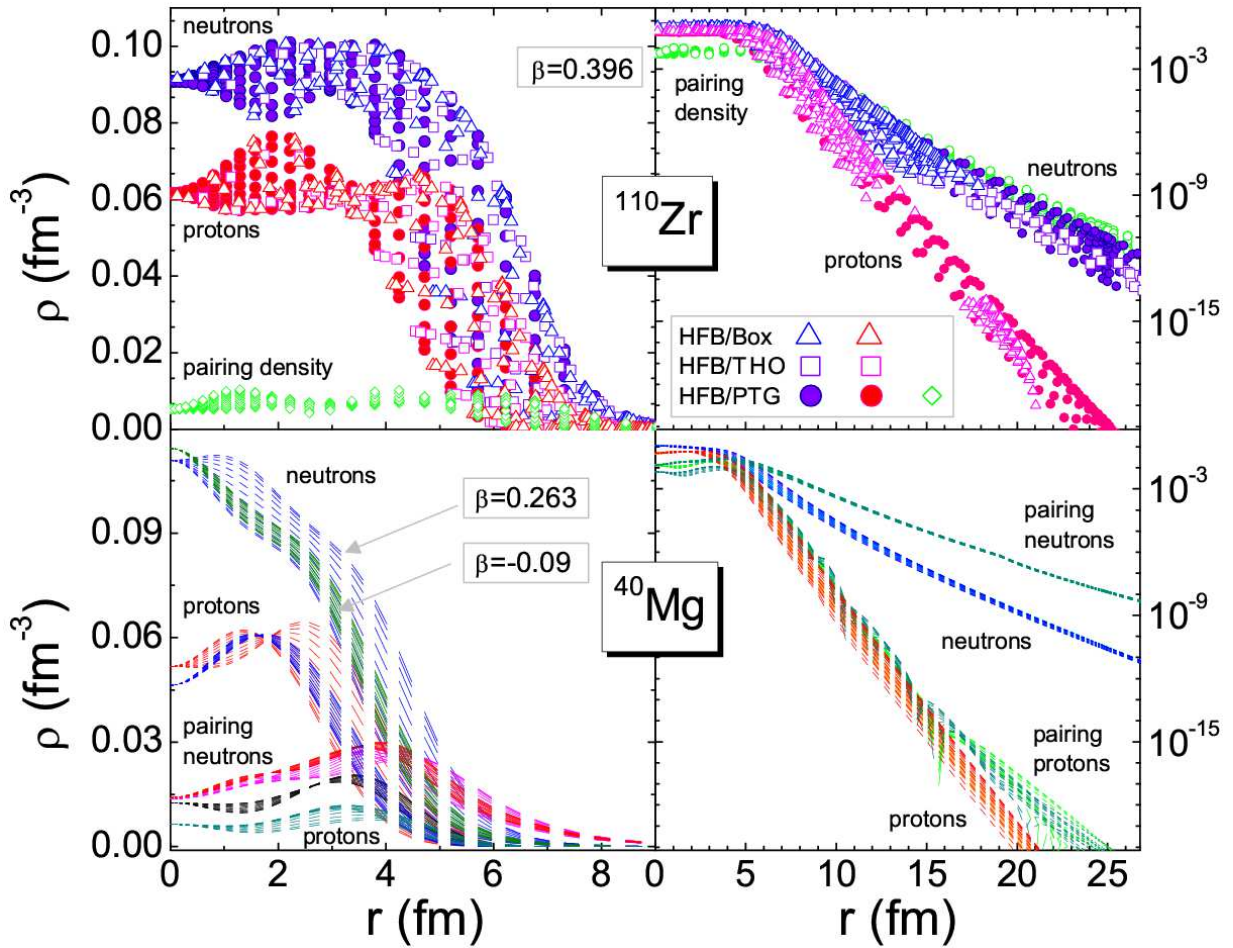


FIG. 8: (color online) The neutron and proton densities of the prolately deformed nucleus ^{110}Zr ($\beta \approx 0.396$), calculated by the HFB/PTG (circles), HFB/Box (triangles), and HFB/THO (squares) methods in normal (top left) and logarithmic (top right) scale. The neutron pairing density (diamonds) is also given for reference. Different curves in the same group represent densities in different directions with respect to the symmetry axis. The neutron and proton densities of ^{40}Mg calculated by the HFB/PTG method for two states with different (oblate and prolate) deformations in normal (bottom left) and logarithmic (bottom right) scale. Different curves in the same group represent densities in different directions with respect to the symmetry axis.

and neutron pairing densities for nuclei ^{110}Zr (top row panels) and ^{40}Mg (bottom row panels) is given in Fig. 8 in normal scale (left column panels) and logarithmic scale (right column panels).

Open circles in the top left panel of Fig. 8 represent the HFB/PTG results, which are compared with the HFB/Box calculations in coordinate space using the Vanderbilt B-spline method (solid circles) and the HFB/THO results (open squares). Diamond symbols stand for the HFB/PTG neutron pairing density. One can see a good agreement between the results of different calculations.

The same comparison, but in logarithmic scale, is given in the top right panel of Fig. 8. The proton HFB/Box result is not available for radial distances around 14-15 fm but just before the box boundary (20 fm), it agrees well with the HFB/PTG density. This comparison confirms the presence of the deformation effect even in the far

asymptotic region, which is accurately taken into account in the HFB/PTG calculations. The same statement applies for the neutron HFB/PTG densities which extend much further than the box radius. The HFB/THO neutron density shows less deformation dependence in the asymptotic region, which is not surprising since all THO basis states have the same asymptotic form.

The bottom row panels of Fig. 8 just illustrate the HFB/PTG normal and pairing densities for two states with different deformations for the drip-line nucleus ^{40}Mg . These states have pairing in both neutron and proton channels. Particle densities can be easily identified because the prolate deformation is larger in magnitude than the oblate deformation and the particle densities associated with the prolate state have larger dispersion at the same value of the radial coordinate r . The prolate and oblate states lead to asymptotic densities which are almost indistinguishable, as seen from the bottom right

panel in Fig. 8.

VI. CONCLUSIONS

We have proposed a new method of the CHFB calculation for spherical and axially deformed nuclei, which properly takes the continuum into account. The method combines configuration-space diagonalization of the HFB Hamiltonian in the complete set of analytical PTG and Bessel/Coulomb wave functions with a matching procedure in the coordinate space which restores the correct asymptotic properties of the HFB wave functions. The PTG potential is chosen to fit the nuclear HF potential and effective mass. The resulting PTG wave functions are close to the bound and continuum states of the related HF potential while the resonance states are substituted by the bound PTG states with shifted single-particle energies. Partial waves of high angular momentum are very well represented by Bessel/Coulomb wave functions.

The main results of the present work are twofold:

First, we have obtained a new scheme (HFB/PTG) to solve the CHFB equations as a promising tool for large-scale calculations; its performance is comparable to that of the HFB/THO code, for example. It properly takes the nuclear continuum into account and therefore could be used for precise density functional calculations for nuclei close to the drip lines. This HFB/PTG method can also be used to provide accurate quasiparticle wave functions for microscopic calculations of dynamics beyond the nuclear mean-field approximation, as for example, the QRPA calculations for deformed nuclei.

Second, the fact that the HFB/PTG calculation reproduces the results of the coordinate-space HFB calculation with the box boundary condition (HFB/Box) even for nuclei up to the neutron drip lines is important. This result indicates the validity of the HFB/Box calculation which is widely used, although its validity is sometimes questioned when it is applied to the drip-line phenomena where continuum effects are crucially important.

The inclusion of resonant structure in the basis is crucial for the success of the HFB/PTG approach. Our test calculations indicate significant disagreement with the HFB/Box result if the PTG bound states representing the resonant GHF states are removed from the basis: in their absence, the pairing densities are overestimated in the surface region, while particle densities are slightly underestimated in the inner region. This means that the resonance states significantly contribute to the total energy through both the particle-hole and particle-particle channels. Their contributions to the pairing correlation energy are evaluated to be about 2-3 MeV for the case of Ni isotopes close to the neutron drip line.

A more complete investigation of the importance of the HFB resonance states could be made by a detailed comparison with the result of the exact Gamow-HFB calculation. Such an analysis is in progress for spherical nuclei and will be reported in the near future [30].

Acknowledgments

The authors acknowledge the Japan Society for the Promotion of Science for awarding the Invitation Fellowship for Research in Japan (Long-term) to M. S. and the JSPS Postdoctoral Fellowship for Foreign Researchers to N. M., which make our collaboration possible. This work was supported by the JSPS Core-to-Core Program ‘‘International Research Network for Exotic Femto Systems.’’ This work was carried out as a part of the U.S. Department of Energy under Contract Nos. DE-FG02-96ER40963 (University of Tennessee), DE-AC05-00OR22725 with UT-Battelle, LLC (Oak Ridge National Laboratory), and DE-FG05-87ER40361 (Joint Institute for Heavy Ion Research), the UNEDF SciDAC Collaboration supported by the U.S. Department of Energy under grant No. DE-FC02-07ER41457.

APPENDIX A: PTG BASIS

1. PTG potential

The one-body Hamiltonian for the exactly solvable PTG model reads:

$$H_{PTG} = \frac{\hbar^2}{2m_0} \left(-\frac{d}{dr} \frac{1}{\mu(r)} \frac{d}{dr} + \frac{\ell(\ell+1)}{r^2 \mu(r)} \right) + V_{PTG}(r) \quad (A1)$$

with m_0 the particle-free mass, r is the radial coordinate (in fm), $\mu(r)$ its dimensionless effective mass (the full effective mass is $m_0 \mu(r)$), ℓ its orbital angular momentum, and $V_{PTG}(r)$ is the PTG potential. The potential $V_{PTG}(r)$ and the effective mass $\mu(r)$ are written:

$$\mu(r) = 1 - a(1 - y^2), \quad (A2)$$

$$V_{PTG}(r) = \frac{\hbar^2 s^2}{2m_0 \mu(r)} \times (V_\mu(r) + V_\ell(r) + V_c(r)), \quad (A3)$$

where V_μ is the potential part issued from the effective mass, V_ℓ its ℓ -dependent part and, V_c its main central

part, defined by

$$\begin{aligned} V_\mu(r) &= [1 - a + [a(4 - 3\Lambda^2) \\ &\quad - 3(2 - \Lambda^2)] y^2 \\ &\quad - (\Lambda^2 - 1)(5(1 - a) + 2ay^2) y^4] \\ &\quad \times \frac{a}{\mu(r)^2} (1 - y^2) [1 + (\Lambda^2 - 1)y^2], \end{aligned} \quad (\text{A4})$$

$$\begin{aligned} V_\ell(r) &= \ell(\ell + 1) \left[\frac{(1 - y^2)(1 + (\Lambda^2 - 1)y^2)}{y^2} \right. \\ &\quad \left. - \frac{1}{s^2 r^2} \right], \quad r > 0, \end{aligned} \quad (\text{A5})$$

$$\begin{aligned} V_c(r) &= (1 - y^2) [-\Lambda^2 \nu(\nu + 1) \\ &\quad - \frac{\Lambda^2 - 1}{4} (2 - (7 - \Lambda^2)y^2 \\ &\quad - 5(\Lambda^2 - 1)y^4)]. \end{aligned} \quad (\text{A6})$$

The quantities $V_{PTG}(r)$ and $\mu(r)$ depend on an implicit function $y = y(r)$ defined in the following way:

$$\Lambda^2 s r = \operatorname{arctanh}(y) + \sqrt{\Lambda^2 - 1} \operatorname{arctan}(\sqrt{\Lambda^2 - 1} y) \quad (\text{A7})$$

so that $0 \leq y < 1$ for $0 \leq r < \infty$.

The numerical solution of Eq. (A7) by way of Newton/bisection methods is stable but one should take special care at large distances when y becomes closely equal to one. For example, this can be done by rewriting Eq. (A7), introducing the new variable $x = \operatorname{arctanh}(y)$:

$$\Lambda^2 s r = x + \sqrt{\Lambda^2 - 1} \operatorname{arctan}(\sqrt{\Lambda^2 - 1} \tanh(x)). \quad (\text{A8})$$

It is solved with respect to x with a fixed-point algorithm. In this region, $1 - y^2$ should be calculated in terms of the expression $1 - y^2 = 4e^{-2x}/(1 + e^{-2x})^2$ to avoid numerical cancellations.

One has to mention that in the calculation of $V_{PTG}(r)$, $V_\ell(r)$ is finite for all $r \geq 0$ but is the difference of two diverging terms for $r \rightarrow 0$. Thus, to be precise in this region, Eq. (A7) must be rewritten as a power series in y , so that the main diverging terms of Eq. (A5) cancel analytically.

As seen from the equations above, there are four parameters in the PTG model: the effective mass parameter a , the scaling parameter s , the parameter Λ determining the shape of the potential, and the parameter ν associated with the depth of the potential. They can take different values for different angular momenta ℓ . We can use this freedom in order to approximate the nuclear potential for each ℓj -subspace, as described in Sec. II.

2. PTG states

The PTG wave functions and eigen-energies are determined by the Schrödinger equation for the Hamiltonian

(A1)

$$H_{PTG} \Psi_k(r) = E \Psi_k(r) \quad (\text{A9})$$

with energies

$$E = \frac{\hbar^2 k^2}{2m_0}, \quad (\text{A10})$$

where s is the scaling parameter and k stands for the complex linear momentum associated with E .

For bound states, if they exist, the parameter ν determines the maximal value n_{max} of the radial quantum number $n = 0, 1, 2, \dots, n_{max}$ as the largest integer inferior to

$$\left\{ \frac{1}{2} \left(\nu - \ell - \frac{3}{2} \right) \right\}, \quad (\text{A11})$$

and defines the complex momentum

$$k_{nl} = is \frac{-A_{nl} + \sqrt{\Delta_{nl}}}{1 - a}, \quad (\text{A12})$$

with

$$A_{nl} = 2n + \ell + \frac{3}{2}, \quad (\text{A13})$$

$$\begin{aligned} \Delta_{nl} &= \Lambda^2 \left(\nu + \frac{1}{2} \right)^2 (1 - a) \\ &\quad - [(1 - a)\Lambda^2 - 1] A_{nl}^2. \end{aligned} \quad (\text{A14})$$

For continuum states, k can take any real positive values from zero to infinity.

3. PTG wave functions

In order to express the PTG wave function $\Phi_k(r) = r \Psi_k(r)$ in a closed analytical form, let us introduce the following three functions

$$f_k(r) = F \left(\nu^-, \nu^+, \ell + \frac{3}{2}, x^- \right) (x^+)^{\bar{\beta}/2}, \quad (\text{A15})$$

$$f_k^+(r) = F \left(\nu^-, \nu^+, \bar{\beta} + 1, x^+ \right) (x^+)^{\bar{\beta}/2}, \quad (\text{A16})$$

$$f_k^-(r) = F \left(\mu^-, \mu^+, -\bar{\beta} + 1, x^+ \right) (x^+)^{-\bar{\beta}/2} \quad (\text{A17})$$

and

$$\chi_k(r) = \sqrt{\frac{x^- + \Lambda^2(1 - a)x^+}{\sqrt{x^- + \Lambda^2 x^+}}} (x^-)^{\frac{\ell + \frac{3}{2}}{2}}, \quad (\text{A18})$$

where

$$x = \frac{1 - (\Lambda^2 + 1)y^2}{1 + (\Lambda^2 - 1)y^2}, \quad x^- = \frac{1 - x}{2}, \quad x^+ = \frac{1 + x}{2}, \quad (\text{A19})$$

$$\nu^+ = \frac{\ell + \frac{3}{2} + \bar{\beta} + \bar{\nu}}{2}, \quad \nu^- = \frac{\ell + \frac{3}{2} + \bar{\beta} - \bar{\nu}}{2}, \quad (\text{A20})$$

$$\mu^+ = \frac{\ell + \frac{3}{2} - \bar{\beta} + \bar{\nu}}{2}, \quad \mu^- = \frac{\ell + \frac{3}{2} - \bar{\beta} - \bar{\nu}}{2}, \quad (\text{A21})$$

$$\bar{\beta} = -\frac{ik}{\Lambda^2 s}, \quad (\text{A22})$$

$$\bar{\nu} = \sqrt{(\nu + 1/2)^2 + \bar{\beta}^2(1 - \Lambda^2(1 - a))}, \quad (\text{A23})$$

and $F(a, b, c, z)$ is the Gauss hypergeometric function [23] (see also Ref. [32] for a recent implementation of the Gauss hypergeometric function and PTG wave functions).

In the case of bound states, k_{nl} determines the momenta k which are purely imaginary (see Eq. (A12)), while they are real positive numbers in the case of scattering states. This defines all other quantities entering the equations above. For both cases, the PTG wave functions can be written either as

$$\Phi_k(r) = \mathcal{N} \chi_k(r) f_k(r) \quad (\text{A24})$$

or as

$$\Phi_k(r) = \mathcal{N} \chi_k(r) (A^+ f_k^+(r) + A^- f_k^-(r)). \quad (\text{A25})$$

Equation (A24) is suitable for numerical work for small distances since $x^- \rightarrow 0$ when $r \rightarrow 0$ so that one is away from the pole of the hypergeometric function appearing at $x^- = 1$. Similarly, Eq. (A25) is applicable for large distances since $x^+ \rightarrow 0$ when $r \rightarrow \infty$ and the pole $x^+ = 1$ of the hypergeometric function in Eqs. (A16) and (A17) is avoided.

In the case of bound states, the quantum numbers $\{nl\}$ are the principal quantum number n and the angular momentum ℓ . The constants \mathcal{N}, A^+, A^- entering Eqs. (A24) and (A25) are given by:

$$\begin{aligned} \mathcal{N} &= \sqrt{\frac{2\Lambda^2 s \bar{\beta} (\ell + \frac{3}{2} + \bar{\beta} + 2n)}{(\ell + \frac{3}{2} + \bar{\beta} \Lambda^2(1 - a) + 2n)}} \\ &\times \sqrt{\frac{\Gamma(\ell + \frac{3}{2} + \bar{\beta} + n) \Gamma(\ell + \frac{3}{2} + n)}{\Gamma(n + 1) \Gamma(\bar{\beta} + n + 1) \Gamma(\ell + \frac{3}{2})^2}}, \\ A^+ &= \frac{\Gamma(\ell + \frac{3}{2}) \Gamma(-\bar{\beta})}{\Gamma(\mu^+) \Gamma(\mu^-)}, \quad A^- = 0, \end{aligned} \quad (\text{A26})$$

where $\Gamma(z)$ is the gamma function [23].

In the case of scattering states, the quantum numbers $\{k\ell\}$ include the momentum k and the angular momen-

tum ℓ , while the associated constants \mathcal{N}, A^+, A^- read:

$$\begin{aligned} \mathcal{N} &= \sqrt{\frac{\Gamma(\nu^+) \Gamma(\nu^-) \Gamma(\mu^+) \Gamma(\mu^-)}{2\pi \Gamma(\bar{\beta}) \Gamma(-\bar{\beta}) \Gamma(\ell + \frac{3}{2})^2}} \\ A^+ &= \frac{\Gamma(\ell + \frac{3}{2}) \Gamma(-\bar{\beta})}{\Gamma(\mu^+) \Gamma(\mu^-)} \\ A^- &= \frac{\Gamma(\ell + \frac{3}{2}) \Gamma(\bar{\beta})}{\Gamma(\nu^+) \Gamma(\nu^-)}. \end{aligned} \quad (\text{A27})$$

The normalization constant \mathcal{N} is determined from the normalization condition

$$\int_0^\infty \Phi_{nl}(r) \Phi_{n'l}(r) dr = \delta_{nn'} \quad (\text{A28})$$

for bound states and from the Dirac delta function normalization for scattering states:

$$\int_0^\infty \Phi_{kl}(r) \Phi_{k'l}(r) dr = \delta(k - k') \quad (\text{A29})$$

All bound and scattering wave functions are orthogonal to each other

$$\int_0^\infty \Phi_k(r) \Phi_{k'}(r) dr = 0, \quad k \neq k' \quad (\text{A30})$$

and they form a complete basis

$$\begin{aligned} &\sum_{nl} \Phi_{nl}(r) \Phi_{nl}(r') \\ &+ \sum_l \int_0^\infty \Phi_{kl}(r) \Phi_{kl}(r') dk = \delta(r - r'). \end{aligned} \quad (\text{A31})$$

One can check that at large distances

$$x \rightarrow -1 + 2e^{-2\Lambda^2 s(r-r_1)}, \quad r \rightarrow \infty, \quad (\text{A32})$$

where

$$\Lambda^2 s r_1 = \sqrt{\Lambda^2 - 1} \arctan(\sqrt{\Lambda^2 - 1}) - \log\left(\frac{\Lambda}{2}\right). \quad (\text{A33})$$

Substituting this into Eq. (A25), one obtains the asymptotic form of the PTG wave functions

$$\Phi_k(r) \mapsto C^+ e^{ikr} + C^- e^{-ikr} \quad (\text{A34})$$

where $C^+ = \mathcal{N} A^+ e^{-ikr_1}$ and $C^- = \mathcal{N} A^- e^{ikr_1}$, defined by Eqs. (A26) and (A27).

The PTG wave functions are numerically stable and accurate when using Eq. (A24) up to $y \leq 0.99$, then applying the form (A25). They accurately land onto their asymptotic representation of Eq. (A34) at large distances.

APPENDIX B: MATRIX ELEMENTS

Let us deal with numerical integration in r and k space. The integration in the r space is performed in terms of N_r Gauss-Legendre integration points x_i and weights w_i within the interval $[0, R_{max}]$,

$$\begin{aligned} & \int_0^\infty O(r) \Phi_k(r) \Phi_{k'}(r) dr \\ &= \sum_{i=1}^{N_r} O(r_i) \Phi_k(r_i) \Phi_{k'}(r_i) w_i, \end{aligned} \quad (\text{B1})$$

where $O(r)$ is an arbitrary function of r , and R_{max} is a point where the nuclear potential disappears. Usually a value $R_{max} = 15$ fm is used. In the same way, integration in the k space is done in terms of N_k Gauss-Legendre integration points k_i and weights w_{k_i} within the interval $[0, k_{max}]$,

$$\begin{aligned} & \int_0^{k_{max}} O(k) \Phi_k(r) \Phi_{k'}(r') dk \\ &= \sum_{i=1}^{N_k} O(k_i) \Phi_{k_i}(r) \Phi_{k_i}(r') w_{k_i}, \end{aligned} \quad (\text{B2})$$

where $O(k)$ is an arbitrary function of k .

Radial integrals must be calculated cautiously due to the presence of non-integrable scattering states in the basis. When the radial operator represents the nuclear potential or explicitly depends on nuclear densities or currents, one can safely integrate the matrix elements to some large but finite distance R_{max} . Beyond R_{max} , the contribution of the integral becomes negligible due to the presence of the densities or currents. However, it is not the case for the kinetic + Coulomb part of the Hamiltonian. This operator is infinite-ranged and induces Dirac delta functions in the matrix elements, which have to be regularized directly. For this, one separates the matrix element in two integrals, defined on the intervals $[0 : R_{max}]$ and $[R_{max} : +\infty[$. The first part is finite and treated with standard methods. For the second part, if one deals with Bessel/Coulomb wave functions, one can assume that the nuclear part is negligible after R_{max} so that they are solutions of the asymptotic HF equations. Hence, one obtains:

$$\begin{aligned} & \int_{R_{max}}^{+\infty} u_\alpha(r) h(r) u_\beta(r) dr \\ &= k_\alpha^2 \left(\delta_{\alpha\beta} - \int_0^{R_{max}} u_\alpha(r) u_\beta(r) dr \right) \text{ (bound)} \\ &= k_\alpha^2 \left(\delta(k_\alpha - k_\beta) - \int_0^{R_{max}} u_\alpha(r) u_\beta(r) dr \right) \text{ (scat)} \\ &= -k_\alpha^2 \int_0^{R_{max}} u_\alpha(r) u_\beta(r) dr \text{ (mixed)} \end{aligned} \quad (\text{B3})$$

where $h(r)$ is the HF potential which reduces to the kinetic + Coulomb Hamiltonian asymptotically. Here,

“bound” (“scat”) means that both α and β states are bound (scattering) and “mixed” means that α is bound and β scattering or vice-versa. The Dirac delta with a discretized basis becomes $\delta_{\alpha\beta}/w_{k_\alpha}$ with w_{k_α} being the Gauss-Legendre weight associated to the discretized value k_α , so that its implementation is immediate; since all integrals are finite, they pose no problem. When the PTG basis states are used instead of the Bessel/Coulomb wave functions, it turns out that it is numerically precise to disregard the Coulomb/centrifugal part of the Hamiltonian after R_{max} , so that Eq. (B3) is the same for both the PTG and Bessel/Coulomb wave functions. Indeed, Eqs. (A32) and (A34) imply that the PTG wave functions behave asymptotically like neutron waves functions of angular momentum $\ell = 0$. The above seemingly crude approximation can, in fact, be mathematically justified. The HFB matrix evaluated using such a procedure converges weakly to the exact HFB matrix for $R_{max} \rightarrow +\infty$ [33]. This means that the HFB matrix elements depend on R_{max} asymptotically, some of them even diverging with $R_{max} \rightarrow +\infty$, whereas its eigenvalues and eigenvectors converge to a finite value.

-
- [1] A. Bulgac, Preprint FT-194-1980, Central Institute of Physics, Bucharest, 1980; nucl-th/9907088.
- [2] J. Dobaczewski, H. Flocard, and J. Treiner, Nucl. Phys. **A422**, 103 (1984).
- [3] J. Dobaczewski, W. Nazarewicz, T.R. Werner, J.F. Berger, C.R. Chinn and J. Dechargé, Phys. Rev. C **53**, 2809 (1996).
- [4] B. Gall, P. Bonche, J. Dobaczewski, H. Flocard and P.-H. Heenen, Z. Phys. **A348**, 183 (1994).
- [5] J. Terasaki, H. Flocard, P.H. Heenen and P. Bonche, Nucl. Phys. **A621**, 706 (1997).
- [6] M. Yamagami, K. Matsuyanagi and M. Matsuo, Nucl. Phys. **A693**, 579 (2001).
- [7] P.-G. Reinhard, M. Bender, K. Rut, and J.A. Maruhn, Z. Phys. **A358**, 277 (1997).
- [8] N. Tajima, RIKEN Review **19**, 29 (1998).
- [9] N. Tajima, Phys. Rev. C **69**, 034305 (2004).
- [10] E. Terán, V.E. Oberacker and A.S. Umar, Phys. Rev. C **67**, 064314 (2003).
- [11] V.E. Oberacker, A.S. Umar, E. Terán and A. Blazkiewicz, Phys. Rev. C **67**, 064302 (2003).
- [12] D. Gogny, Nucl. Phys. **A237**, 399 (1975).
- [13] M. Girod and B. Grammaticos, Phys. Rev. C **27**, 2317 (1983).
- [14] J.L. Egido, H.-J. Mang, and P. Ring, Nucl. Phys. **A334**, 1 (1980).
- [15] J.L. Egido, J. Lessing, V. Martin and L.M. Robledo, Nucl. Phys. **A594**, 70 (1995).
- [16] J. Dobaczewski and P. Olbratowski, Comput. Phys. Commun. **158**, 158 (2004).
- [17] M.V. Stoitsov, J. Dobaczewski, W. Nazarewicz and P. Ring, Comput. Phys. Commun. **167**, 43 (2005).
- [18] S. Goriely, M. Samyn, P.-H. Heenen, J. M. Pearson and F. Tondeur, Phys. Rev. C **66**, 024326 (2002).
- [19] P. Ring, Prog. Part. Nucl. Phys. **37**, 193 (1996).
- [20] M.V. Stoitsov, J. Dobaczewski, W. Nazarewicz, S. Pittel and D.J. Dean, Phys. Rev. C **68**, 054312 (2003).
- [21] N. Michel, W. Nazarewicz and M. Ploszajczak, Phys. Rev. C **75**, 031301 (2007).
- [22] J. Ginocchio, Ann. of Phys. **159**, 467 (1985).
- [23] M. Abramowitz and I.A. Stegun, *Handbook of Mathematical Functions* (Dover, New York, 1970).
- [24] N. Michel, Comp. Phys. Comm., **176**, 232 (2007).
- [25] I.J. Thomson and A.R. Barnett, Comp. Phys. Comm. **36**, 363 (1986).
- [26] A. Blazkiewicz, V.E. Oberacker, A.S. Umar and M. Stoitsov, Phys. Rev. C **71**, 054321 (2005).
- [27] E. Chabanat, P. Bonche, P. Haensel, J. Meyer and F. Schaeffer, Nucl. Phys. **A635**, 231 (1998).
- [28] M. Grasso, N. Sandulescu, Nguen Van Giai and R.J. Liotta, Phys. Rev. C **64**, 064321 (2001).
- [29] M. Yamagami, Phys. Rev. C **72**, 064308 (2005).
- [30] N. Michel, M. Stoitsov and K. Matsuyanagi, in preparation.
- [31] K. Bennaceur and J. Dobaczewski, Comp. Phys. Comm. **168**, 96 (2005).
- [32] N. Michel and M. Stoitsov, arXiv:0708.0116
- [33] "Principles of Functional Analysis", Martin Schechter, Second Edition, American Mathematical Society, 2001